Applied Surface Science 722 (2026) 165537

Contents lists available at ScienceDirect

Applied Surface Science

journal homepage: www.elsevier.com/locate/apsusc

Full Length Article

Hydrogen plasma treated iron vanadate nanoparticles for efficient ammonia sensing

Pelin Kavraz [a], Aman Bhardwaj [b], Thomas Fischer [b], Ivo Kuritka [c], David John Dmonte [c,d,*], Sanjay Mathur [b,*], Namık Akcay [e,**]

[a] Department of Physics, Institute of Graduate Studies in Sciences, Istanbul University, Fatih, 34116 Istanbul, Turkey
[b] Institute of Inorganic and Materials Chemistry, University of Cologne, Greinstr. 6, 50939 Cologne, Germany
[c] Centre of Polymer Systems, Tomas Bata University in Zlín, Tr. Tomase Bati 5678, 760 01 Zlín, Czech Republic
[d] New Technologies – Research Centre, University of West Bohemia in Pilsen, 8 Univerzitní, Pilsen 301 00, Czech Republic
[e] Department of Physics, Faculty of Science, Istanbul University, 34314 Vezneciler, Istanbul, Turkey

ARTICLE INFO

Keywords:
Gas sensing
Iron vanadate
Hydrogen plasma
Ammonia sensor
Nanoparticles

ABSTRACT

In this study, we investigate the impact of hydrogen plasma treatment on the gas-sensing properties of iron vanadate ($FeVO_4$) nanostructures. The $FeVO_4$ nanoparticles were synthesized via a sol–gel method, followed by surface modification using hydrogen plasma. Both hydrogen plasma-treated (hp-$FeVO_4$) and untreated ($FeVO_4$) samples were systematically characterized using X-ray diffraction (XRD), scanning electron microscopy (SEM), and X-ray photoelectron spectroscopy (XPS) techniques. Gas sensing experiments revealed that hp-$FeVO_4$ nanostructures exhibited a response to 50 ppm NH_3 that was twice as high as that of untreated $FeVO_4$ samples, highlighting the significant enhancement achieved through plasma surface engineering. Notably, the hp-$FeVO_4$ sensor exhibited a response time of 72 s and a recovery time of 292 s, operating at a reduced temperature of 380 °C, possibly due to increased band bending on the plasma-treated surface. Moreover, the sensor exhibited promising repeatability, selectivity, and long-term stability without the need to incorporate noble metals. These findings highlight the strong potential of hydrogen plasma-modified iron vanadate for advanced gas sensing applications.

1. Introduction

Ammonia occurs naturally as organic matter decomposes and through the metabolic activities of specialised bacteria in the nitrogen cycle, as well as from volcanic activity [1,2]. It is typically colourless and has a sharp, pungent odour [3]. There is substantial use of ammonia in the chemical industry, commonly as a refrigerant, and also in certain clinical diagnostic procedures. Moreover, the majority of global ammonia production serves as a precursor in the chemical synthesis of nitrogen-containing compounds in chemical engineering, or in the production of fertilizers for the agricultural sector, which is essential to ensuring global food security [4,5]. However, it should be approached carefully due to its possible harmful effects on human health [6]. In particular, the Occupational Safety and Health Administration states that being exposed to 35 ppm of ammonia for 10 min is the upper safety limit for humans [7,8]. Regardless of the relatively low ammonia content in the atmosphere which is between 0,001–0,005 ppm [9], the risk of pollution in the air and aquatic environment caused by the usage of ammonia should be monitored by the agricultural and industrial sectors [10]. Ammonia-containing waste generated by the agricultural sector is caused by contaminants, animal excrement, or the release of fertilizers into seas or oceans, which greatly threatens aquatic life [2]. When it comes to the harmful effects of the substance on the human body, ammonia can be fatal depending on the level of exposure. Ammonia is corrosive to skin, eyes, and visceral organs; hence, it may cause deep burns, blindness, and even internal bleeding and coma, which may lead to death at high levels, while at lower concentrations it remains harmful, at least as an irritant. [11]. As the world fosters alternative energy sources, ammonia is proposed as a strong candidate as an intermediary fuel source for hydrogen. Apart from advancing the existing transport and global storage systems due to its importance as a fertiliser, it is predicted to double production in the next decade and

* Corresponding authors.
** Corresponding author.
E-mail addresses: dmonte@ntc.zcu.cz (D.J. Dmonte), sanjay.mathur@uni-koeln.de (S. Mathur), akcay@istanbul.edu.tr (N. Akcay).

https://doi.org/10.1016/j.apsusc.2025.165537
Received 4 September 2025; Received in revised form 7 December 2025; Accepted 9 December 2025
Available online 10 December 2025

even rise up to 100 times as energy demands are anticipated to scale up significantly in the longer term [12]. Additionally, ammonia feedback sensors are in widespread usage in diesel engines, which minimises the hazardous nature of NO_x emissions by selective catalytic reduction since it is a good source of hydrogen [8,13]. Considering such crucial aspects in this research direction, it becomes a requirement to detect ammonia accurately in the environment and other potential industrial applications.

In recent research, two-dimensional transition-metal dichalcogenides (TMDCs) have demonstrated how engineered nanosheets and heterostructures provide faster charge transport and enable contemporary sensor platforms that approach real-time detection with high selectivity at room temperature, although this material requires a multi-step synthesis procedure [14–16]. However, it is well established that semiconductor materials yield great performance in gas sensing operations thanks to their high thermal and electrical stabilities [17,18]. Considering a relatively wide band gap (~2.2 eV) and better stability properties, vanadium oxides have drawn more attention recently [19,20]. In particular, iron vanadate ($FeVO_4$), which is a promising n-type semiconductor material, has shown excellent applicability in areas such as catalysts [21], solar water splitting [22], lithium-ion batteries [23], and is one of the well-studied materials in gas sensing applications since it possesses a uniquely sensitive electrical property [24]. As with the boost in surface area is generally directly linked to advanced gas sensing properties, nanosized particles have been shown to yield better performance compared to the bulk form of the material. In this implication, some studies have been conducted regarding the gas sensing property of $FeVO_4$; Kaneti et al. [25] states that the porous $FeVO_4$ nanorods synthesized by the hydrothermal method give the best results in n-butanol gas sensing at 270 °C. Similarly, Lehnen et al. [26] prepared a film by using $FeVO_4$ nanorods and concluded that the material is also favorable for oxygen sensing. $FeVO_4$ has also been used for ammonia detection before by Qi Lu et al., who analysed Ag-decorated $FeVO_4$ particles as sensing electrode material in ammonia sensing and obtained great results in terms of repeatability, selectivity, and stability at 550 °C [27]; They have also studied the $FeVO_4$ material by doping different molar ratios of metal oxides (NiO, SnO_2, WO_3). These modified materials were used as a YSZ-based mixed potentiometric sensor, and the 20 mol. % NiO modified $FeVO_4$ showed the best detection range of 53–83 mV versus 100 ppm NH_3 [28]. This means that, to date, very few reports exist on the use of metal vanadate nanomaterial sensors to detect ammonia. Moreover, their sensitivity in potentiometric applications had to be elevated using noble metal nanoparticle decorations. However, the sensing properties can also be enhanced by the presence of oxygen vacancies on the material's surface. Conventionally, oxygen vacancy or surface defect density can be engineered by hydrogen or oxygen plasma treatment, which is a feasible and well-established technology. Thus, plasma treatment can be performed to increase oxygen vacancies [29,30].

Indeed, the plasma treatment technique is a reliable method for modifying the features of nanomaterials [31,32]. This method modifies the surface properties of the nanostructure without disturbing the single-crystal structure [33]. For example, different plasma gases (oxygen, hydrogen, nitrogen, and argon) treated tin oxide thick film gas sensors were studied and the oxygen plasma-treated sensor was found to have the highest relative response towards tested gases, but it was poorly selective, whereas hydrogen plasma treated sensor showed good selectivity and sensitive to CO gas [34]. The SnO_2 gas sensors that have been subjected to plasma treatment became sensitive to propanol at ambient temperature, and the relative response improved over time as they were exposed to oxygen and hydrogen gaseous plasma [35]. The reduction of graphene oxide by hydrogen plasma at ambient temperature led to the creation of a carbon dioxide gas sensor [36]. It has also been proven that the hydrogen plasma effect improves the photoelectrochemical performance [37].

Unlike the above-mentioned recent potentiometric approaches, the chemiresistive principle for gas sensing is probably the most straightforward and feasible sensor design. To the best of our knowledge, there are no reports available on the use of purely $FeVO_4$ based nanomaterial as a chemiresistive sensor for ammonia gas. Moreover, we hypothesise that the material is prone to sensitivity enhancement by hydrogen plasma, which may be more favourable than the incorporation of noble metals or other nanodecorations on its surface. Therefore, in this work, the chemiresistive sensing layer of $FeVO_4$ was synthesised directly on the substrate using the sol–gel method and then treated with hydrogen plasma. The gas sensing properties of $FeVO_4$ and plasma-treated sensor $FeVO_4$ (hp-$FeVO_4$) were measured towards ammonia gas in the air. The hp-$FeVO_4$ exhibited significantly improved sensing characteristics, including a high response rate to NH_3 gas detection, low operating temperature, and high relative response (relative change from the sensor's initial resistance, given in %). Finally, a plausible sensing mechanism for the proposed hp-$FeVO_4$ sensor to NH_3 is also discussed. This work demonstrates the great potential of hydrogen plasma-treated iron vanadate for mainstream ammonia detection.

2. Experimental section

2.1. Materials synthesis

The $FeVO_4$ nanoparticles were synthesised using the sol–gel method. Iron nitrate, $Fe(NO_3)_3.6(H_2O)$ dissolved in distilled water, and ammonium metavanadate NH_4VO_3, dissolved in warm distilled water, were mixed together and stirred for 2 h using a magnetic stirrer. The resulting orange precipitate was repeatedly washed with distilled water and ethanol. A tube furnace was used to calcine the solid precipitate in air at 600 °C for 2 h. The resulting material was used for characterisation and sensing measurements.

2.2. Characterization techniques

The crystalline phases of both samples were characterized by powder X-ray diffraction (XRD) using a STOE STADI MP device with Mo-Kα radiation ($\lambda = 0.07093$ nm). The surface morphology and particle size of the materials were examined using a scanning electron microscope (FE-SEM). The chemical bonding state of elements present in powders was investigated by X-ray photoelectron spectroscopy (XPS) using an ESCA M−probe Spectrometer (Surface Science Instruments), at a pressure in the 10^{-9} mbar range, equipped with a monochromatic Al Kα excitation source (1486.6 eV). The powders were loaded onto standard powder sample holders and always left in a preparation chamber for degassing for several hours prior to measurement. The resolution step size was set to 0.25 eV for the survey spectra, while the high-resolution spectra were recorded at a step of 0.05 eV. The Photoelectron pass energy is set to 158.3 eV for the survey scans and it is set to 55.2 eV for narrow scans of high resolution measurements. An electron flood gun was used to reduce the surface charging of the sample. The position of the adventitious carbon C 1 s line was used to determine the binding energies (BE). For insulating samples, the related inaccuracy of the correction (BE estimation) method ranges from 0.1 eV to 0.2 eV [38]. Spectral calibration and peak fitting were performed using CasaXPS software. The backgrounds were corrected with a Shirley line shape.

2.3. Sensor fabrication and ammonia detection

The prepared powder material was mixed with an α-terpinol solution by 10 wt%, and ultrasonic treatment was performed for 30 min using a VWR Ultrasonic Cleaner device (model USC300T). An amount of 10 μL from the mixed solution was carefully dropped onto the 4-pin TO39 sensor structure (UST Umwelt Sensor Technik GmbH) sensor structure. At least three sensors were prepared with the same method for each material, and all sensors were dried for 24 h to ensure a smooth surface. In order to obtain long-term stability, the sensors were sintered at 500 °C

for 45 min. For SEM analysis, see Fig. S11 in the supplementary document.

For hydrogen plasma treatment, one of the sintered $FeVO_4$ sensors was exposed to an RF plasma chamber equipped with a power generator of 200 W. The sensors were placed for 20 min under the constant flow of 20 sccm H_2 gas.

Gas detection measurements of the prepared samples were carried out on custom-built gas detection equipment connected to a computer with the required control units. Resistivity measurements were performed using LabView software operating in an interface with a Keithley 2400 source measuring device. The sensor temperature was controlled using another custom-developed LabView software for using the power supply (ES-PS 3065-03B- Elektro Automatik) with a predefined voltage curve. Another Lab View application is developed for operating the airflow system and collecting experimental data. The samples were placed in a stainless-steel chamber with two connections (inlet/exhaust) with a volume of 250 ml. The mass flow control (Aera FC-7700C) was used to keep the accurate gas flow rate in the chamber. A dry air cylinder (certified for 0 % humidity) supplied by Air Products and Chemicals, Inc., was used to prevent the exposure of the sensor surface to ambient moisture. Ammonia (NH_3 – 0.05 % + 99.95 N_2) was used for the analysis of the sample, and other reference gases methane (CH_4 – 0.1 % + 99.99 N_2), carbon monoxide (CO – 0.1 %, 99.99 N_2) were used to test the relative response against different gases. All pre-mixed analyte gases supplied by Air Products and Chemicals, Inc. (certified for 0 % humidity) and by combining the flow of the target gas with the flow of dry air, the desired concentrations as tested below were achieved.

To determine the relative response (100.ΔR) of the $FeVO_4$ sensor toward reducing and oxidizing gases, Eqs. (1) and (2), respectively were used.

$$RelativeResponse(\%) = 100 \bullet \Delta R = \frac{Ra - Rg}{Ra} \bullet 100 \quad (1)$$

$$RelativeResponse(\%) = 100 \bullet \Delta R = \frac{Rg - Ra}{Ra} \bullet 100 \quad (2)$$

Here, *Ra* is the resistance of the sensor in the synthetic air, and *Rg* is the sensor's resistance to target gases. T_{90} response and T_{90} recovery time are defined as the duration of time required for the sensor to reach 90 % of the total resistance [39,40].

For the sake of clarity, mathematical simplicity yielding a straight-line graphical representation, and conformity with the power-law model adopted from the literature [41], the ratio of the sensor's resistance in synthetic air to that in the target gas (*Ra/Rg*) is used in the corresponding text and figure in Section 3.2.

3. Results and discussion

3.1. Physicochemical properties

The XRD patterns of pristine $FeVO_4$ and hydrogen plasma-treated exhibit (Fig. 1) diffraction peaks corresponding with the PDF file number 038–1372 with some minor visible crystalline impurities, which might be due to the minor presence of metallic VO_x or FeO_x phases. This suggests the formation of $FeVO_4$ in a triclinic crystal system with a P-1 (2) space group. The major diffraction peaks at 2θ (2-theta) of 7.59°, 9.21°, 10.65°, 11.43°, 12.38°, 12.64°, 14.23°, 15.14° 15.99°, 16.83°, 17.59°, 19.02° and 19.55° matched the (1 1 0), ($\bar{1}$11), ($\bar{2}$10), (1 2 0), (0$\bar{1}$2), ($\bar{2}$20), ($\bar{2}\bar{2}$1), (1 2 1), ($\bar{2}$12), (1$\bar{3}$2), ($\bar{2}$31), ($\bar{3}$30) and ($\bar{3}$22) *hkl* crystal planes that verified the formation of $FeVO_4$ [42,43]. The average sizes (D) of the coherently diffracting areas were calculated with the Debye-Scherrer equation D = kλ/B cosθ [44]. Assuming approximately isometric crystallites, the k value is set to 0.94. The values obtained for D are 109 nm and 97 nm for the untreated control $FeVO_4$ and plasma-treated $FeVO_4$ samples, respectively.

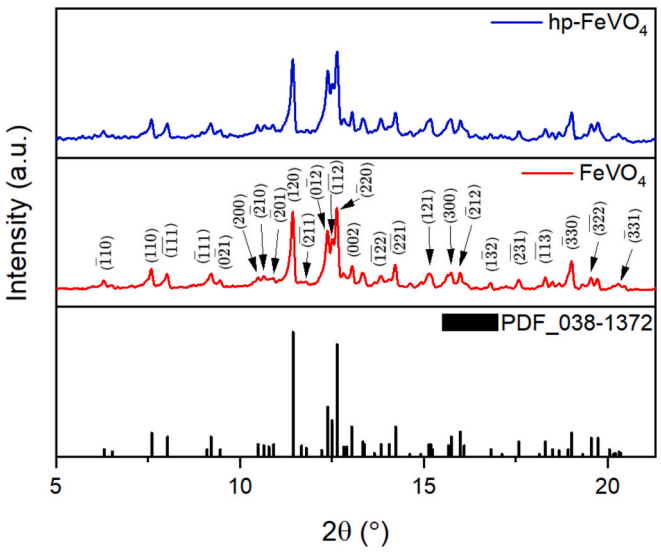

Fig. 1. The XRD patterns of $FeVO_4$ and hp-$FeVO_4$ samples.

The average size of the $FeVO_4$ nanoparticles is approximately 170 nm, and they exhibit an oblong shape with some agglomeration effects as evident in the SEM micrograph in Fig. 2(a). The graphs of particle size distribution are shown in the supplementary document's Figs. S3 and S4. The samples exposed to hydrogen plasma revealed that the nanocrystals generally tend to be more separated, and also that the larger aggregates appear to have broken down into smaller grains. The measured average particle size after plasma treatment was approximately 130 nm (Fig. 2b), indicating a significant reduction in overall particle size. The observed reduction in crystallite size is supported by the average crystallite size D analysed from the XRD data. The hydrogen plasma treatment can also help eliminate residual solvent molecules and alter surface charges, reducing particle agglomeration and, as a consequence, improving uniformity of the sensing surface, similar to these physical effects discussed elsewhere [45]. It can also enhance surface charge carrier concentration and facilitate more possible interactions between the sensor material and gas molecules, thereby improving detection performance [29,36].

X-ray photoelectron spectroscopy (XPS) analysis was performed to confirm the presence of elements and their elemental binding state on the surface. Fig. 3(a) demonstrates that the high-resolution spectrum of Fe 2p shows two peaks corresponding to the orbital splitting into Fe $2p_{3/2}$ and Fe $2p_{1/2}$ at 711.5 eV and 725.4 eV, respectively. This can be observed in both the $FeVO_4$ and hp-$FeVO_4$, although there seems to be a very minor shift resulting in both the Fe $2p_{3/2}$ and Fe $2p_{1/2}$ orbitals to 711.8 eV and 725.5 eV, leading to an energy separation (D ¼ 13.7 eV) which is denotative of the formation of Iron (III) oxide [46]. This is well within the expected error resolution of our instrument. These peaks confirm the existence of Fe^{3+} in both nanomaterials [27]. Moreover, the evidence of the shoulder peak and minor satellite peaks in the hydrogen plasma-treated sample is characteristic of the minor yet observable occurrence of Fe^{2+} centers. This could be due to the reduction of Fe^{3+} to Fe^{2+} as described in this previously published work [47].

The C 1 s high-resolution spectrum in Fig. 3(b) has a broad peak that can be deconvoluted into three peaks at 284.6 eV, 285.9 eV, and 287.9 eV for $FeVO_4$, and 284.8 eV, 286.3 eV, and 288.8 eV for hp-$FeVO_4$ corresponding to C–C, C-OH/C-OR, and O=C-O, respectively [48]. In Fig. 3(c) the high-resolution spectra of both $FeVO_4$ and hp-$FeVO_4$ confirm the vanadium in + 5 oxidation state, due to the orbital splitting into V $2p_{3/2}$ peak observed at 517 eV and V $2p_{1/2}$ peak observed at 524 eV accordingly [49]. The peaks at 522.6 eV and 520.3 eV before the plasma treatment sample have shown peak broadening, probably because of the Coster-Kronig effect [50]. The peak shifting from 524.4

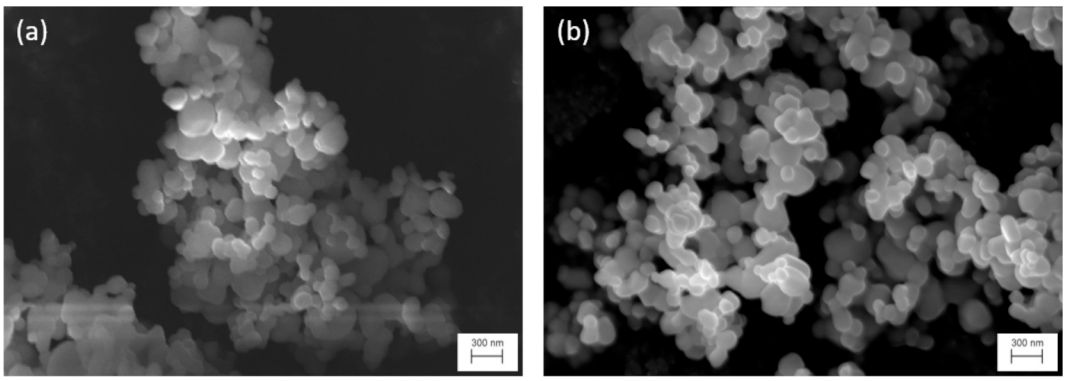

Fig. 2. The SEM images of (a) $FeVO_4$ and (b) hp-$FeVO_4$ nanoparticles.

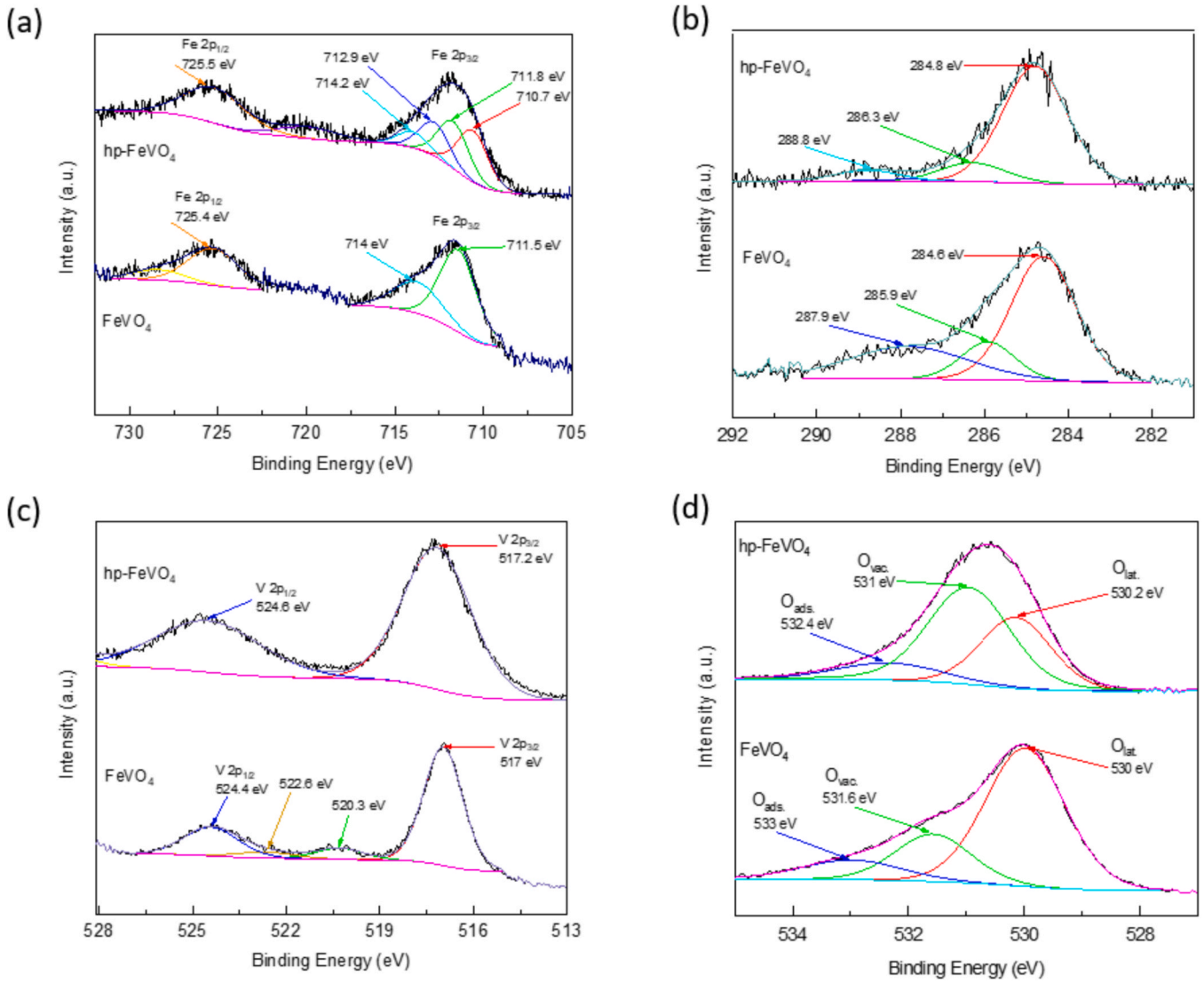

Fig. 3. High-resolution X-ray photoelectron spectroscopy scans of (a) Fe 2p b) C 1 s c) V 2p d) O 1 s in $FeVO_4$ and hp-$FeVO_4$ samples.

eV, 522.6, and 520.3 eV to 524.6 eV is credited to hydrogen plasma treatment. The untreated sample $FeVO_4$ shows additional peaks at 522.6 eV and 520.3 eV, which generally indicate lower oxidation states of vanadium, like V^{4+} and maybe V^{3+}, as discussed in [51]. In contrast, the hydrogen plasma-treated sample seems to show diminished lower oxidation states of vanadium. This could be due to conserving electroneutrality. The deconvoluted peaks for O 1 s plotted in Fig. 3(d), for both $FeVO_4$ and hp-$FeVO_4$ samples, exhibit characteristic peaks corresponding to lattice oxygen at binding energies of 530 eV and 530.2 eV, respectively. The second most pronounced signal O 1 s component at higher-BE component (~531 eV) is conventionally denoted O_{vac} and is associated to oxygen atoms in defect-rich or under-coordinated

environments in the vicinity of oxygen-vacancy sites while XPS does not probe the vacancy itself. A small O 1 s contribution at the higher BE (above 532 eV) can be attributed the adsorbed oxygen species or residual hydroxides denoted as O_{ads}. The significant enhancement of the hp-$FeVO_4$ sensor's oxygen vacancy concentration and the slight decrease of the adsorbate component may lead to an improvement in the relative response of the gas sensor [52].

3.2. Gas sensing properties

Gas sensing measurements were performed by measuring the electrical resistance of the device under variable thermodynamic conditions, such as temperature and gas concentrations. To determine the optimum temperature, measurements were performed in both $FeVO_4$ and hp-$FeVO_4$ sensors exposed to 50 ppm NH_3 gas with a 20 °C step in the temperature range between 340 °C- 440 °C. As the sensor reached a stable baseline at each temperature level, ammonia-containing gas was introduced into the chamber. The operating temperature strongly influences the response/recovery time of a semiconductor oxide sensor, and the chemical activity of the sensor shall be fully stimulated at the right operating temperature [53]. Fig. 4(a) shows that the relative response of both $FeVO_4$ and hp-$FeVO_4$ sensors exposed to 50 ppm NH_3 (airflow = 200 sccm) gradually increases with increasing temperature. The relative response of hp-$FeVO_4$ reaches its maximum at 380 °C, with subsequent temperature increases causing the relative response to further diminish. The same effect was observed for the $FeVO_4$ sensor after 420 °C.

When the sensor is operated at temperatures lower than the chosen optimum of 380 °C. The reaction rate will be slow, and the response will be low because the energy is insufficient to overcome the activation energy. As the temperature rises, the electrochemical processes get accelerated, and a higher response value is obtained. Further, when the operating temperature exceeds the optimum value, the gas adsorption capacity decreases, and the gas molecules can be released without interacting with the sensor, resulting in a reduced response time [27,54]. When the $FeVO_4$ and hp-$FeVO_4$ sensors are compared, the sensor without hydrogen plasma treatment reached a maximum relative response of 28 % while the hp-$FeVO_4$ sensor, with the effect of hydrogen plasma, showed a relative response of 54 %, which is approximately two times higher at a relatively lower temperature. The baseline response to dry air of both nanomaterials is also shown in Fig. 4(a), and as expected, the baseline resistance (Ra) of both $FeVO_4$ and hp-$FeVO_4$ decreases when the temperature increases from 340 °C to 440 °C, which is in line with the typical behaviour of semiconductor materials. It can be seen that hp-$FeVO_4$ shows much higher baseline resistance, about 5 times higher than $FeVO_4$. This hydrogen plasma treatment is known to modify the electronic band gap structure as shown by Peng et al [55]. The creation of vacancy clusters in our nanomaterial is conceivable to induce mid-gap states, as discussed previously in this work by Andreas et al [47]. Further potential plasma-induced grain boundary effects, as discussed by Aadesh et al [37], and a plausible polaron hopping mechanism, as described in the literature by Anju et al [56], in combination, seem to have widened the depletion-layer width and thereby increased the baseline resistance [57]. It is worth noting that the increase in the sensor's baseline resistance due to plasma treatment is a promising feature, assuming the sensor responds to the target gas by decreasing its resistance. In order to clearly show the relative response variation, a nonlinear fitting was drawn on both the sensing data to clearly observe the peak response as the operating temperature. Therefore, further experiments were conducted on the hp-$FeVO_4$ sensor with the optimum operating temperature of the sensor set to 380 °C as this factor allows for optimum gas detection performance. Fig. 4(b) shows the transient response of the sensor towards a pulse of 50 ppm NH_3. For the hp-$FeVO_4$ sensor, when 50 ppm NH_3 gas is released into the system for 100 s, with a total airflow of 200 sccm. The response and recovery times are 72 and 292 s making the total sensing cycle time 364 s.

The continuous response and recovery curves of the hp-$FeVO_4$ sensor to test its repeatability are given in Fig. 5(a) under the gas flow of 50 ppm NH_3 at 380 °C. The sensor showed a median T_{90} response time of 51 s and a median T_{90} recovery time of 523 s for 4 consecutive cycles, indicating reasonable reproducibility. The related values and calculations are shown in Tables S1 and S2 in the supplementary document.

To verify whether the change in gas concentration affects the hp-$FeVO_4$ relative response and to also investigate LOD (Limit of Detection), NH_3 gas was introduced into the chamber with a constant increase in the range of 5–80 ppm for 100 s and the results were recorded as shown in Fig. 5(b). Measurements were taken by keeping the airflow constant at 800 sccm in order to reach low ppm values as per our system design. As can be clearly seen, the relative response tends to increase gradually with increasing NH_3 concentration. The relative responses of the sensor towards 5, 10, 20, 40, and 80 ppm ammonia were recorded as 4 %, 16 %, 28 %, 38 % and 43 % respectively. Compared to the standard deviation of the signal noise in Fig. 5(b), it can be assumed that the 5 ppm is just the LOD demonstrated, being ca three times higher than the standard deviation.

The n-type semiconductor oxide-based gas sensor responds to a reducing gas analyte in air atmosphere by resistance changes following a power law for the *Ra/Rg* ratio [41]:

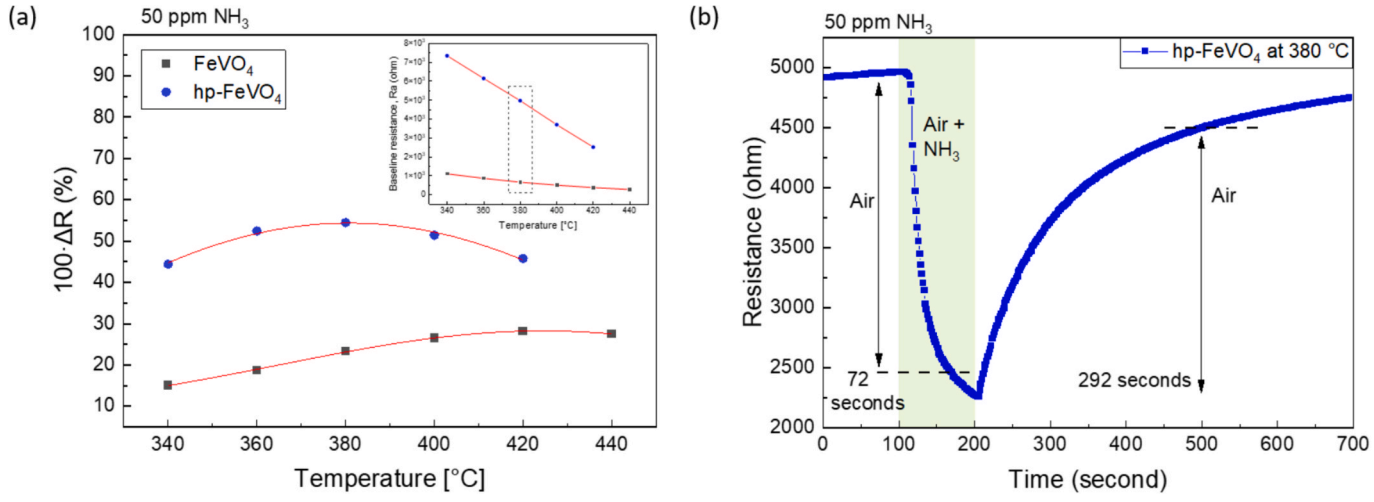

Fig. 4. (a) Relative response and baseline resistance of $FeVO_4$ and hp-$FeVO_4$ sensors as a function of temperature, (b) Exemplary response of hp-$FeVO_4$ at operating temperature showing T_{90} Response/recovery time.

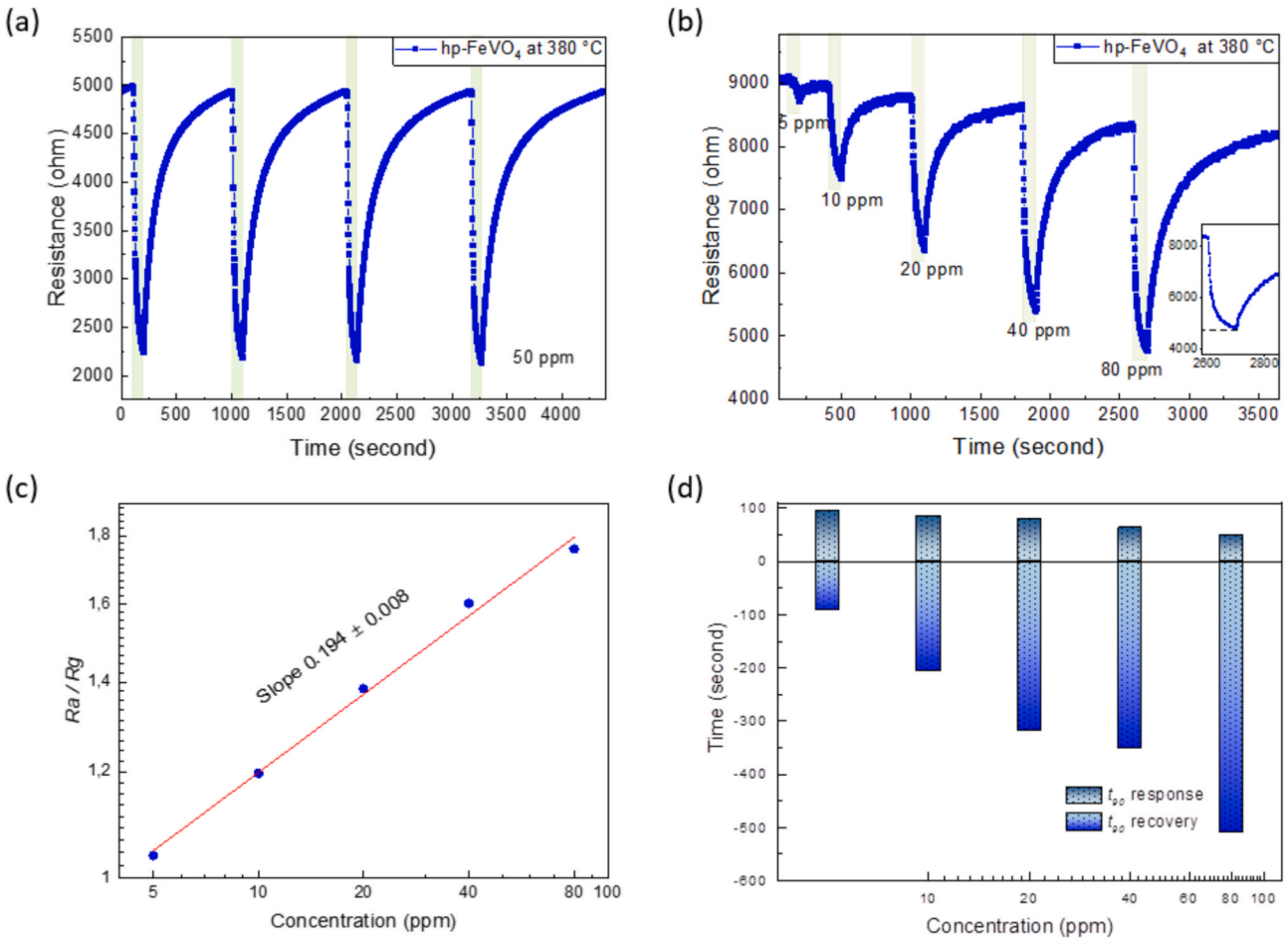

Fig. 5. (a) Repeatability measurements with 50 ppm NH_3 at operating temperature (b) Response and recovery transient response curves of the hp-$FeVO_4$ across NH_3 concentration (c) Linear fit of the sensor Ra/Rg ratio plotted against NH_3 exposure concentration at the operating temperature (d) Response/recovery dynamics across NH_3 concentration range.

$$\frac{Ra}{Rg} \propto a[C]^b \tag{3}$$

where *Ra* and *Rg* are of the meaning already defined in the experimental section, *C* is the concentration of the target gas (in ppm), *a* is the scaling factor and *b* is the exponent, both are constants for a given sensor at the operating temperature. In more detail, *b* is a surface ion charge related parameter depending on the type of the material and on the charge state of the chemisorbed oxygen species, usually around 0.5 for O^{2-} and 1 for O^-. To estimate the character of oxygen ion species adsorbed on the surfaces of the sensor, the sensor response can be replotted in log–log coordinates as shown in Fig. 5(c), so the parameter *b* corresponds to the slope of the linear relationship and can be obtained by simple linear fitting. Accordingly, a *b* value of 0.194 ± 0.008 was obtained which is closer to 0.5 rather than 1. This implies O^{2-} ions are the prevailing form of surface adsorbed oxygen species which matches well with the expectation for temperatures above 300 °C [58]. The hydrogen plasma treatment may also reduce some of the surface metal centers to Fe^{2+} or create oxygen vacancies, and possibly, a minor magnetite phase change on the surface. This allows for the electron hopping possibility between octahedral Fe^{2+} and Fe^{3+}, which results in higher conductivity and, therefore, higher response [47]. The surface oxygen species then reacts with the ammonia gas, thereby increasing conductivity, which is detected while maintaining the same rate of diffusion. As shown in the sensing cycle graphs, the plasma-treated sensor produces a much higher response, possibly due to the release of more electrons into the conduction band of the nanomaterial, enabling a rapid response to ammonia gas during the sensing process. On the other hand, it appears to be a tradeoff with the longer recovery process of the sensing cycle, which is the inverse replacement of the filling of the surface vacancies by the oxygen species. Fig. 5(d) demonstrates the T_{90} response and recovery time changes depending on the gas concentration. As the gas concentration increases, more gas atoms react with the sensor surface per unit time, which affects the carrier's concentration. Accordingly, the response time increases with the absorption of more gas atoms. The sensor reaches saturation when all the atoms on its surface interact with the target gas, and the increase in absorbed gas atoms causes an increase in the recovery time [59,60].

In order to determine the selectivity of the hp-$FeVO_4$ sensor to other gases (CO, CH_4), the test was carried out by providing gas flow into the chamber for 100 s under a constant airflow of 200 sccm at an operating temperature of 380 °C. The results are shown in Fig. 6(a). hp-$FeVO_4$ sensor exhibits significantly higher selectivity towards NH_3 gas as compared to CO and CH_4 gases. This is demonstrated by its proportionally larger response to NH_3 even when other gases are tested at double the analyte concentrations individually. This selective behaviour allows for the reliable detection of NH_3 gas in specific environments, minimising cross-sensitivity issues with CO or CH_4 gas. The sensor showed the highest relative response with 54 % to 50 ppm analyte NH_3 gas. The long-term stability of the sensor at constant conditions (50 ppm NH_3, 380 °C) was investigated as shown in Fig. 6(b). The results show that the sensor demonstrated reasonably good stability over 56 days.

The good selectivity to NH_3 over CO and CH_4, and a stable response at 380 °C in dry air indicate that hp-$FeVO_4$ can tolerate sustained

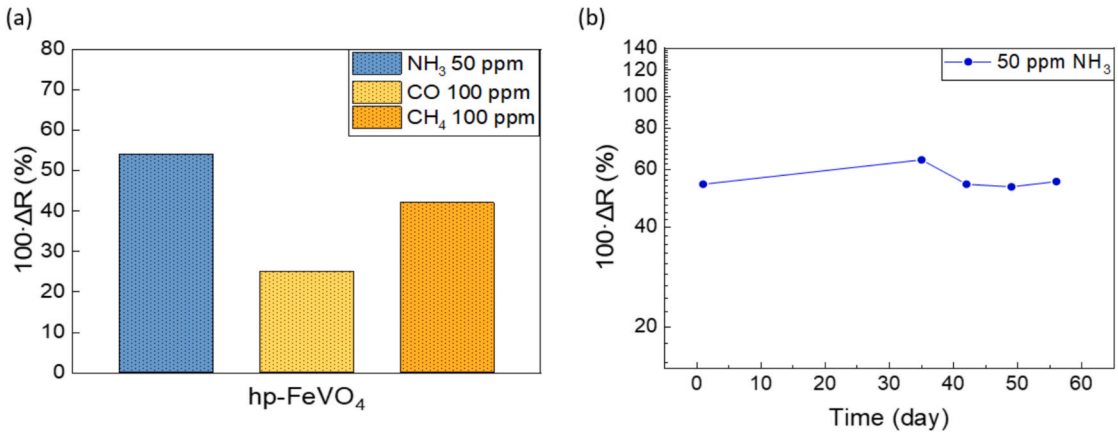

Fig. 6. (a) Gas selectivity bar graph for hp-$FeVO_4$ at operating temperature, (b) Long-term stability to 50 ppm NH_3 of the sensor.

high-temperature operation, which is just one of the many prerequisites for potential testing towards exhaust-related environments, while other future studies remain to verify the suitability of this material for such demanding applications. Nevertheless, the high-temperature NH_3 monitoring has high potential application in industrial or agricultural environments with less reactive atmospheres, where robustness, long-term stability, and insensitivity to ambient humidity are valued more than ultra-low detection limits [27,61–63].

3.3. Gas sensing mechanism

The electronic conduction of $FeVO_4$ is known to show n-type semiconductor behaviour [21,52]. The change in resistance results from the reaction between the target gas and the oxygen species on the material's surface. The synthetic air, which is the carrier gas, moving through the chamber, allows the oxygen species to react with the $FeVO_4$ surface. The absorbed oxygen species capture free electrons from the conduction band of material, forming chemically absorbed oxygen species (O_2^-, O^{2-}, O^-). This causes the energy band-bending and creates a depletion layer. As the carrier concentration on the material surface decreases, the resistance of the sensor increases until a balance is achieved with the ambient oxygen atmosphere (baseline resistance) [64,65].

$$O_{2_{(ads)}} + e^- \longleftrightarrow O^-_{2(ads)} \tag{4}$$

$$O^-_{2(ads)} + e^- \longleftrightarrow 2O^-_{(ads)} \tag{5}$$

$$O^-_{(ads)} + e^- \longleftrightarrow O^{2-}_{(ads)} \tag{6}$$

The introduced surface and near-surface oxygen vacancies also modify local band bending, which is directly linked to gas adsorption and desorption kinetics. Plasma-induced vacancies are known to be particularly effective, as their density and spatial distribution can be precisely tuned via plasma parameters such as duration, power, and gas composition [66,67]. In other words, the plasma treatment allows the creation of ions and free radicals, which are chemically active species that react with one another. As a result, it creates a composition of single, multiple, positive, negative, and charged species and electrons [57]. In hydrogen plasma, the ionic species include H^+, H_2^+, H_3^+ etc, and hydrogen radicals as well. The hydrogen plasma creates a reducing effect on the lattice oxygen, thus generating oxygen vacancies on the metal oxide surface. As the hydrogen plasma exposure time increases, a decrease in lattice oxygen occurs and donates electrons to the bulk, thus reducing the bulk's resistance [34,68].

$$H^+ + H^+ + 2e^- \longleftrightarrow H_2 \tag{7}$$

$$H_2 + O_{ad} \longleftrightarrow H_2O \tag{8}$$

$$H^+ + O_{lat} + e^- \longleftrightarrow (O_{lat}H) \tag{9}$$

The intergranular connections on the surface can be accessed by ambient gases due to the surface porosity of the $FeVO_4$. Therefore, we assume that the partial gas concentration and the depletion layer that forms on the surface of the grains competitively exert their influence and affect the material property. As a result, the hp-$FeVO_4$ increased surface area and reduced particle size and agglomeration, allowing for more access to grain boundaries and, henceforth, showing improved relative response [69]. Therefore, we can assume that the conduction mechanism of the sensing layer, along with imperfect small and large grains with connective necks, which affect grain-grain transfer, plays a crucial role in the overall conduction mechanism. Thus, a combination of the surface bulk model, grain boundary model, and the nanocrystal model, as described by Barsan et al., along with the effects of surface-level band bending, is highly probable to explain the overall sensing mechanism of the $FeVO_4$ material before and after hydrogen plasma treatment [70] (See Fig. 7).

Ammonia, as a reducing gas, provides additional electrons to induce a near-surface deposition layer responsible for increased conductivity [34,35]. In our system environment, oxygen ions are adsorbed onto the surface, and electron transfer occurs from the surface. The loss of electrons causes a potential barrier between neighbouring grains and creates an electron depletion layer, which increases the resistance to the flow of electrons across grain boundaries in the *off*-phase of the cycle. However, when the sensor is exposed to NH_3, the oxygen anions react with the gas, providing the grains with a substantial number of electrons. Consequently, as the electron depletion layer shrinks, the energy barrier between adjacent crystal grains decreases, enabling greater electron flow manifested as a decrease in resistivity. In other words, electrons must exceed the surface band bending to participate in the conduction process [71,72]. The band bending change was calculated from the conductometric sensing performance for the n-type material as follows;

$$q\Delta V = -k_B T In\left(\frac{R_{air}}{R_{NH_3}}\right) \tag{10}$$

where $q\Delta V$ is the change in the band bending, k_B is the Boltzmann constant, T is the temperature, R_{air} is the sensor resistance in air environment, R_{NH_3} is the sensor resistance in NH_3 gas environment [73]. From equation (10), the change in band bending was calculated and plotted in Fig. 8(a) for both $FeVO_4$ and hp-$FeVO_4$ sensors toward 50 ppm NH_3. It shows higher band bending at the lower operating temperature for the hp-$FeVO_4$ sensor, confirming improved gas sensing kinetics. The graph closely resembles Fig. 4(a), except it is flipped along the vertical axis. Hence, the observed trends are in agreement with the proposed mechanism for the given type of semiconductor. Moreover, at the selected operating temperature, the hp-$FeVO_4$ sensor exhibits a

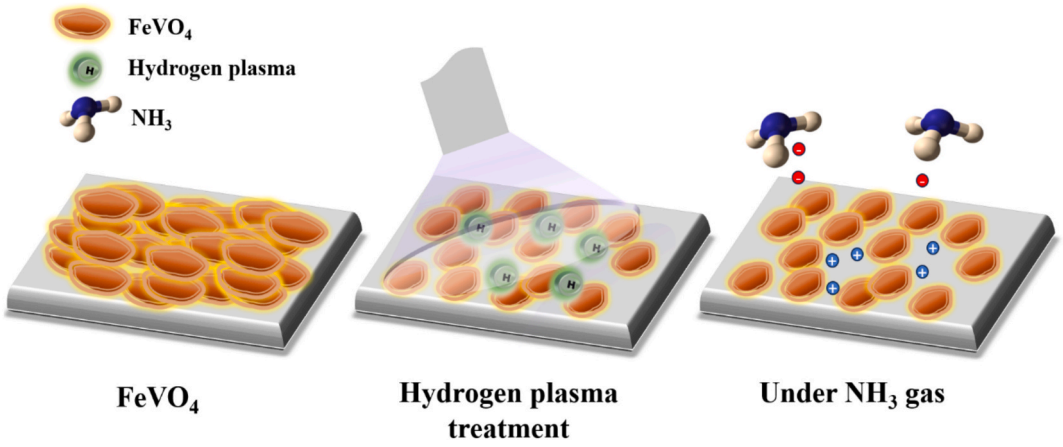

Fig. 7. Schematic of the interaction between $FeVO_4$ and NH_3 treated by hydrogen plasma.

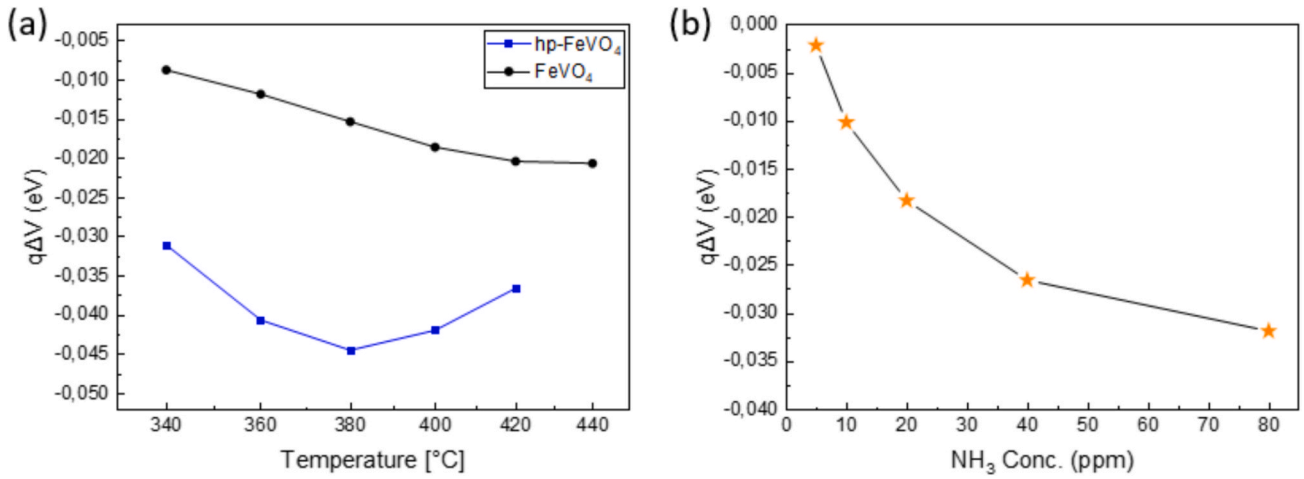

Fig. 8. Changes in band bending (qΔV), (a) with temperature change, b) with increases in NH_3 concentration (5−80 ppm) at 380 °C.

significant increase in surface-level band bending with rising gas concentration. This effect also confirms the proposed mechanism and is evident in the 5–80 ppm range, as shown in the band bending plot in Fig. 8(b).

After NH_3 gas is introduced into the chamber, the target gas molecules interact with the oxygen ions absorbed on the surface of the sensing layer material. This process returns trapped electrons to the conduction band, increasing electron concentration and, therefore, decreasing the overall resistance of the sensor. Although we did not measure any surface reactions, the possible chemical interaction between NH_3 and the oxygen species adsorbed on the surface of $FeVO_4$ can be discussed by the mechanism reported by Lu et al in their research work [28].

Additionally, recent theoretical and computational studies, including density functional theory (DFT) modelling, have discussed and researched the role of oxygen vacancies at defective oxide surfaces in dramatically lowering the activation energy for charge transfer processes, making the sensor more responsive to target gases [74]. At these defective sites, charge transfer between the adsorbed gas molecule and the metal oxide is facilitated, reinforcing the link between the engineered vacancy landscape and improved sensor performance. Together, these effects explain the observed improvements in both the sensitivity and selectivity of hp-$FeVO_4$ sensors compared to their untreated counterparts [75].

3.4. Comparison with other sensing nanomaterials

Since this work presents the first purely $FeVO_4$-based chemiresistive gas sensor of ammonia in air, it cannot be directly compared with other works on this material. However, it is helpful to compare the performance of the hp-$FeVO_4$ with other recently reported works including not only their LOD, but also the operating temperatures, target analytes, and approximate size of characteristic structural features despite the type of sensing. These previous efforts in $FeVO_4$ sensing are summarized in Table 1, demonstrating the full comparability of the material presented here with others, while offering the advantages of a simple chemiresistive sensing principle, lower operating temperature, and the replacement of demanding noble metals or nickel oxide decorations through a simple and cost-effective hydrogen plasma synthesis method. Recently, NH_3 sensors employing trending materials such as TMDCs and hybrid nanocomposites have achieved impressive room-temperature performance, albeit a multi-step and expensive material synthesis process [77–82]. The regime of high-temperature sensing remains advantageous for long-term stability, reversible response, less effects from humidity and selective adsorption–desorption control [83–86]. This hydrogen plasma-treated $FeVO_4$ sensor operates within a moderate thermal range that ensures efficient redox activity and consistent selectivity toward NH_3. It allows for a balance of structural robustness and sensing reliability, which differentiates the present work from emerging low-temperature approaches.

Table 1
Comparison of $FeVO_4$-based sensors and other chemo-resistive nanomaterials for gas sensing.

Sample	LOD	Usage of noble metal	Operating temperature	Target gas	Material size	Relative Response
hp-$FeVO_4$ (present work)	5 ppm	no	380 °C	Ammonia	~130 nm	54 % (50 ppm)
Porous $FeVO_4$ nanorods [25]	10 ppm	no	270 °C	N-butanol	70–270 nm diameter; 0.7–3.5 μm length	8.32 (100 ppm)
$FeVO_4$ nanorods [26]	10 %	no	250 °C	Oxygen	160 nm diameter, 1.5–2 μm length; Pore size 10–30 nm	0.29 ± 0.01 ($m = -3.4 \pm 0.1$) (10–100 %)
Ag decorated $FeVO_4$ [27]	200 ppb	yes	550 °C	Ammonia	0.1–0.5 μm (Ag nanoparticles)	−57 mV (50 ppm)
NiO modified $FeVO_4$ [28]	5 ppm	no	650 °C	Ammonia	~80–100 nm (estimated from SEM)	− 83 mV (100 ppm)
$FeVO_4$ /Pt nanorods [76]	10 ppm	yes	240 °C	N-butylamine	$FeVO_4$ rods (2–3 μm × 50–100 nm) with Pt particles (2–5 nm)	44.6 (40 ppm)
rGO-WO_3 [77]	1.14 ppm	no	35 °C	Ammonia	120–130 nm (WO_3 nanospheres)	15.83 (100 ppm)
rGO–SnO_2 [78]	0.6 ppm	no	RT, 25 °C	Ammonia	~12 nm	4.3 Hz ppm^{-1}(1 ppm)
SnP_x/rGO [79]	43.6 ppb	no	RT, 25 °C	Ammonia	100 nm SnP_x	117.5 % (40 ppm)
$MoSe_2/CeO_2$ [80]	70 ppb	no	RT, 25 °C	Ammonia	flower–like microstructures	45 (1 ppm)
PtO_2-decorated MoS_2 [81]	50 ppm	yes	200 °C	Ammonia	40–100 nm	450 % (500 ppm)
MoS_2 and WS_2 thin films [82]	< 100 ppb	no	30 °C	Ammonia	30–40 nm	0.03 ± 0.0 ppm^{-1} (MoS_2) 0.10 ± 0.02 ppm^{-1} (WS_2) (200 ppb)

4. Conclusions

To summarize, we synthesized iron vanadate nanoparticles using the sol–gel method and fabricated the sensors to detect NH_3 after being treated with hydrogen plasma (hp-$FeVO_4$) in comparison to the control, which is $FeVO_4$. This hp-$FeVO_4$ (hydrogen plasma treated) sensor showed more than 2 times higher relative response to 50 ppm NH_3 with a T_{90} response time of about 72 s when compared with $FeVO_4$. Thus, the exposure to the hydrogen plasma increases the number of adsorption sites and increases band bending on the surface, resulting in an increase in relative response. Further, the gas-sensing performance measurements confirmed that the hp-$FeVO_4$ sensor has good repeatability, selectivity, and maintains its stability for a long time. This proved that the sensor fabricated without the use of noble metals to detect NH_3 gas showed great potential with its low cost and long-lasting stability.

CRediT authorship contribution statement

Pelin Kavraz: Writing – original draft, Methodology, Investigation, Data curation. **Aman Bhardwaj:** Writing – review & editing, Methodology, Investigation. **Thomas Fischer:** Investigation, Formal analysis, Data curation. **Ivo Kuritka:** Writing – review & editing, Investigation. **David John Dmonte:** Writing – review & editing, Methodology, Investigation, Formal analysis. **Sanjay Mathur:** Supervision, Resources, Project administration, Conceptualization. **Namık Akcay:** Writing – review & editing, Supervision, Project administration, Funding acquisition, Formal analysis.

Declaration of competing interest

The authors declare that they have no known competing financial interests or personal relationships that could have appeared to influence the work reported in this paper.

Acknowledgments

This study was funded by the Scientific Research Projects Coordination Unit of Istanbul University. Project number is FYL-2021-38266. In addition, David J. Dmonte confirms the result was created with the financial support of the University of West Bohemia, Czech Republic Motivation System–POSTDOC part. Ivo Kuritka acknowledges the Ministry of Education, Youth and Sports of the Czech Republic for financial support from the DKRVO funds (project No. RP/CPS/2024-28/007). The work was also supported by Operational Programme Johannes Amos Comenius financed by European Structural and Investment Funds and the Czech Ministry of Education, Youth and Sports (Project No. SENDISO - CZ.02.01.01/00/22_008/0004596). The University of Cologne is gratefully acknowledged for all in-kind support provided. Pelin Kavraz and David J. Dmonte specifically acknowledge the ERASMUS + program. We are very grateful to Ziyaad Aytuna, Seulgi Ji, and other researchers from the University of Cologne for their assistance with laboratory work.

Appendix A. Supplementary data

Supplementary data to this article can be found online at https://doi.org/10.1016/j.apsusc.2025.165537.

Data availability

Data will be made available on request.

The data described in the article are available at: 10.5281/zenodo.17523820, and the dataset is available at: 10.5281/zenodo.17580664.

References

[1] H.I. Chen, C.Y. Hsiao, W.C. Chen, C.H. Chang, T.C. Chou, I.P. Liu, K.W. Lin, W. C. Liu, Characteristics of a Pt/NiO thin film-based ammonia gas sensor, Sens Actuators B Chem 256 (2018) 962–967, https://doi.org/10.1016/j.snb.2017.10.032.
[2] D.J. Randall, T.K.N. Tsui, Ammonia toxicity in fish, Mar. Pollut. Bull. 45 (2002) 17–23, https://doi.org/10.1016/S0025-326X(02)00227-8.
[3] J. Pauluhn, Acute inhalation toxicity of ammonia: revisiting the importance of RD_{50} and $LCT_{01/50}$ relationships for setting emergency response guideline values, Regul. Toxicol. Pharm. 66 (2013) 315–325, https://doi.org/10.1016/j.yrtph.2013.05.008.
[4] S.G. Pawar, M.A. Chougule, S.L. Patil, B.T. Raut, P.R. Godse, S. Sen, V.B. Patil, Room temperature ammonia gas sensor based on polyaniline-TiO_2 nanocomposite, IEEE Sens. J. 11 (2011) 3417–3423, https://doi.org/10.1109/JSEN.2011.2160392.
[5] A. Adeniyi, I. Bello, T. Mukaila, N.C. Sarker, A. Hammed, Trends in biological ammonia production, Biotech 12 (2023) 41, https://doi.org/10.3390/biotech12020041.
[6] D.R. Patil, L.A. Patil, P.P. Patil, Cr_2O_3-activated ZnO thick film resistors for ammonia gas sensing operable at room temperature, Sens Actuators B Chem 126 (2007) 368–374, https://doi.org/10.1016/j.snb.2007.03.028.

[7] G.K. Mani, J.B.B. Rayappan, A highly selective and wide range ammonia sensor - nanostructured ZnO:Co thin film, Mater. Sci. Eng. B 191 (2015) 41–50, https://doi.org/10.1016/j.mseb.2014.10.007.

[8] D. Kwak, Y. Lei, R. Maric, Ammonia gas sensors: a comprehensive review, Talanta 204 (2019) 713–730, https://doi.org/10.1016/j.talanta.2019.06.034.

[9] G.K. Mani, J.B.B. Rayappan, A highly selective room temperature ammonia sensor using spray deposited zinc oxide thin film, Sens Actuators B Chem 183 (2013) 459–466, https://doi.org/10.1016/j.snb.2013.03.132.

[10] A. Murawska, P. Prus, The progress of sustainable management of ammonia emissions from agriculture in european union states including poland—variation, trends, and economic conditions, Sustainability (Switzerland) 13 (2021) 1–21, https://doi.org/10.3390/su13031035.

[11] A.G. Bannov, M.V. Popov, A.E. Brester, P.B. Kurmashov, Recent advances in ammonia gas sensors based on carbon nanomaterials, Micromachines (Basel) 12 (2021) 186, https://doi.org/10.3390/mi12020186.

[12] D.R. MacFarlane, P.V. Cherepanov, J. Choi, B.H.R. Suryanto, R.Y. Hodgetts, J. M. Bakker, F.M. Ferrero Vallana, A.N. Simonov, A roadmap to the ammonia economy, Joule 4 (2020) 1186–1205, https://doi.org/10.1016/j.joule.2020.04.004.

[13] D.Y. Wang, S. Yao, M. Shost, J.H. Yoo, D. Cabush, D. Racine, R. Cloudt, F. Willems, Ammonia sensor for closed-loop SCR control, SAE Int J. Passeng. Cars–Electron. Electr. Syst. 1 (2009) 323–333, https://doi.org/10.4271/2008-01-0919.

[14] A. Mirzaei, M. Alizadeh, H.R. Ansari, M. Moayedi, Z. Kordrostami, H. Safaeian, M. H. Lee, T.U. Kim, J.Y. Kim, H.W. Kim, S.S. Kim, Resistive gas sensors for the detection of NH_3 gas based on 2D WS_2, WSe_2, MoS_2, and $MoSe_2$: a review, Nanotechnology 35 (2024) 332002, https://doi.org/10.1088/1361-6528/AD4B22.

[15] X. Li, W. Zeng, S. Zhuo, B. Qian, Q. Chen, Q. Luo, R. Qian, Highly sensitive room-temperature detection of ammonia in the breath of kidney disease patients using $Fe_2Mo_3O_8/MoO_2$@MoS_2 nanocomposite gas sensor, Adv. Sci. 11 (2024), https://doi.org/10.1002/advs.202405942.

[16] Z. Li, Y. Rao, Z. Wang, T. Zhang, G. Wu, L. Sun, Y. Ren, L. Tao, Universal synthesis of core–shell-structured ordered mesoporous transition metal dichalcogenides/metal oxides heterostructures with active edge sites, Small Struct. 6 (2025), https://doi.org/10.1002/sstr.202400376.

[17] G.F. Fine, L.M. Cavanagh, A. Afonja, R. Binions, Metal oxide semi-conductor gas sensors in environmental monitoring, Sensors 10 (2010) 5469–5502, https://doi.org/10.3390/s100605469.

[18] G. Neri, First fifty years of chemoresistive gas sensors, Chemosensors 3 (2015) 1–20, https://doi.org/10.3390/chemosensors3010001.

[19] A. Dhayal Raj, T. Pazhanivel, P. Suresh Kumar, D. Mangalaraj, D. Nataraj, N. Ponpandian, Self assembled V_2O_5 nanorods for gas sensors, Curr. Appl Phys. 10 (2010) 531–537, https://doi.org/10.1016/j.cap.2009.07.015.

[20] Y. Li, Z. Zeng, Y. Chen, Y. Zhang, W. Wang, X. Xu, M. Du, Z. Li, Z. Zou, $FeVO_4$ nanowires for efficient photocatalytic CO_2 reduction, Catal. Sci. Technol. 12 (2022) 3289–3294, https://doi.org/10.1039/d2cy00324d.

[21] J. Deng, J. Jiang, Y. Zhang, X. Lin, C. Du, Y. Xiong, $FeVO_4$ as a highly active heterogeneous Fenton-like catalyst towards the degradation of Orange II, Appl Catal B 84 (2008) 468–473, https://doi.org/10.1016/j.apcatb.2008.04.029.

[22] H. Mandal, S. Shyamal, P. Hajra, A. Bera, D. Sariket, S. Kundu, C. Bhattacharya, Development of ternary iron vanadium oxide semiconductors for applications in photoelectrochemical water oxidation, RSC Adv. 6 (2016) 4992–4999, https://doi.org/10.1039/c5ra22586h.

[23] D. Hao Sim, X. Rui, J. Chen, H. Tan, T.M. Lim, R. Yazami, H.H. Hng, Q. Yan, Direct growth of FeVO4 nanosheet arrays on stainless steel foil as high-performance binder-free Li ion battery anode, RSC Adv. 2 (2012) 3630–3633, https://doi.org/10.1039/c2ra20058a.

[24] V.D. Nithya, R.K. Selvan, C. Sanjeeviraja, D.M. Radheep, S. Arumugam, Synthesis and characterization of $FeVO_4$ nanoparticles, Mater. Res. Bull. 46 (2011) 1654–1658, https://doi.org/10.1016/j.materresbull.2011.06.005.

[25] Y.V. Kaneti, Z. Zhang, J. Yue, X. Jiang, A. Yu, Porous $FeVO_4$ nanorods: synthesis, characterization, and gas-sensing properties toward volatile organic compounds, J. Nanopart. Res. 15 (2013) 1948, https://doi.org/10.1007/s11051-013-1948-z.

[26] T. Lehnen, M. Valldor, D. Nižňanský, S. Mathur, Hydrothermally grown porous $FeVO_4$ nanorods and their integration as active material in gas-sensing devices, J Mater Chem A Mater 2 (2014) 1862–1868, https://doi.org/10.1039/c3ta12821k.

[27] Q. Lu, L. Huang, W. Li, T. Wang, H. Yu, X. Hao, X. Liang, F. Liu, P. Sun, G. Lu, Mixed-potential ammonia sensor using Ag decorated $FeVO_4$ sensing electrode for automobile in-situ exhaust environment monitoring, Sens Actuators B Chem 348 (2021) 130697, https://doi.org/10.1016/j.snb.2021.130697.

[28] Q. Lu, L. Huang, X. Hao, W. Li, B. Wang, T. Wang, X. Liang, F. Liu, C. Wang, G. Lu, Mixed potential type NH_3 sensor based on YSZ solid electrolyte and metal oxides (NiO, SnO_2, WO_3) modified $FeVO_4$ sensing electrodes, Sens Actuators B Chem 343 (2021) 130043, https://doi.org/10.1016/j.snb.2021.130043.

[29] Z. Zhang, L. Zhao, H. Du, J. Chu, Improved NO_2 gas-sensing performance of PPy by hydrogen plasma treatment: experimental study and DFT verification, Sens Actuators A Phys 364 (2023) 114848, https://doi.org/10.1016/j.sna.2023.114848.

[30] Y. Hou, A.H. Jayatissa, Enhancement of gas sensor response of nanocrystalline zinc oxide for ammonia by plasma treatment, Appl. Surf. Sci. 309 (2014) 46–53, https://doi.org/10.1016/j.apsusc.2014.04.158.

[31] H. Wu, X. Bu, M. Deng, G. Chen, G. Zhang, X. Li, X. Wang, W. Liu, A gas sensing channel composited with pristine and oxygen plasma-treated graphene, Sensors (Switzerland) 19 (2019) 625, https://doi.org/10.3390/s19030625.

[32] A.G. Bannov, O. Jašek, A. Manakhov, M. Márik, D. Nečas, L. Zajíčková, High-performance ammonia gas sensors based on plasma treated carbon nanostructures, IEEE Sens. J. 17 (2017) 1964–1970, https://doi.org/10.1109/JSEN.2017.2656122.

[33] J. Pan, R. Ganesan, H. Shen, S. Mathur, Plasma-modified SnO_2 nanowires for enhanced gas sensing, J. Phys. Chem. C 114 (2010) 8245–8250, https://doi.org/10.1021/jp101072f.

[34] A. Chaturvedi, V.N. Mishra, R. Dwivedi, S.K. Srivastava, Selectivity and sensitivity studies on plasma treated thick film tin oxide gas sensors, Microelectron. J. 31 (2000) 283–290, https://doi.org/10.1016/S0026-2692(99)00147-0.

[35] R. Srivastava, R. Dwivedi, S.K. Srivastava, Effect of oxygen and hydrogen plasma treatment on the room temperature sensitivity of SnO_2 gas sensors, Microelectron. J. 29 (1998) 833–838, https://doi.org/10.1016/S0026-2692(97)00117-1.

[36] S. Muhammad Hafiz, R. Ritikos, T.J. Whitcher, N.M. Razib, D.C.S. Bien, N. Chanlek, H. Nakajima, T. Saisopa, P. Songsiriritthigul, N.M. Huang, S. A. Rahman, A practical carbon dioxide gas sensor using room-temperature hydrogen plasma reduced graphene oxide, Sens Actuators B Chem 193 (2014) 692–700, https://doi.org/10.1016/j.snb.2013.12.017.

[37] A.P. Singh, N. Kodan, A. Dey, S. Krishnamurthy, B.R. Mehta, Improvement in the structural, optical, electronic and photoelectrochemical properties of hydrogen treated bismuth vanadate thin films, Int. J. Hydrogen Energy 40 (2015) 4311–4319, https://doi.org/10.1016/j.ijhydene.2015.01.085.

[38] D.J. Miller, M.C. Biesinger, N.S. McIntyre, Interactions of CO_2 and CO at fractional atmosphere pressures with iron and iron oxide surfaces: one possible mechanism for surface contamination? Surf. Interface Anal. 33 (2002) 299–305, https://doi.org/10.1002/sia.1188.

[39] A. Queraltó, D. Graf, R. Frohnhoven, T. Fischer, H. Vanrompay, S. Bals, A. Bartasyte, S. Mathur, $LaFeO_3$ nanofibers for high detection of sulfur-containing gases, ACS Sustain. Chem. Eng. 7 (2019) 6023–6032, https://doi.org/10.1021/acssuschemeng.8b06132.

[40] P. Ghadage, P. Kodam, D. Nadargi, S. Patil, M. Tamboli, N. Bhandari, I. Mulla, C. Park, S. Suryavanshi, Pd loaded bismuth ferrite: a versatile perovskite for dual applications as acetone gas sensor and photocatalytic dye degradation of malachite green, Ceram. Int. 49 (2023) 5738–5747, https://doi.org/10.1016/j.ceramint.2022.10.153.

[41] S. Choopun, A. Tubtimtae, T. Santhaveesuk, S. Nilphai, E. Wongrat, N. Hongsith, Zinc oxide nanostructures for applications as ethanol sensors and dye-sensitized solar cells, Appl. Surf. Sci. 256 (2009) 998–1002, https://doi.org/10.1016/j.apsusc.2009.05.139.

[42] X. He, C. Zhang, D. Tian, The structure, vibrational spectra, and thermal expansion study of AVO_4 (A=Bi, Fe, Cr) and $Co_2V_2O_7$, Materials 13 (2020) 1628, https://doi.org/10.3390/ma13071628.

[43] S. Sharma, V. Dutta, P. Raizada, A. Hosseini-Bandegharaei, V.K. Thakur, A. Singh, Q. Van Le, V.H. Nguyen, P. Singh, Constructing a novel all-solid-state Z-scheme $BiVO_4$/CQDs/$FeVO_4$ photocatalyst and its enhancement to the photocatalytic activity, Mater. Lett. 297 (2021) 129940, https://doi.org/10.1016/j.matlet.2021.129940.

[44] M. Basak, M.L. Rahman, M.F. Ahmed, B. Biswas, N. Sharmin, The use of X-ray diffraction peak profile analysis to determine the structural parameters of cobalt ferrite nanoparticles using Debye-Scherrer, Williamson-Hall, Halder-Wagner and Size-strain plot: different precipitating agent approach, J. Alloys Compd. 895 (2022) 162694, https://doi.org/10.1016/j.jallcom.2021.162694.

[45] P. Dutta, S. Paul, D. Galipeau, V. Bommisetty, Effect of hydrogen plasma treatment on the surface morphology, microstructure and electronic transport properties of nc-Si:H, Thin Solid Films 518 (2010) 6811–6817, https://doi.org/10.1016/j.tsf.2010.06.037.

[46] D. Barreca, G. Carraro, A. Gasparotto, C. Maccato, C. Sada, A.P. Singh, S. Mathur, A. Mettenbörger, E. Bontempi, L.E. Depero, Columnar Fe_2O_3 arrays via plasma-enhanced growth: interplay of fluorine substitution and photoelectrochemical properties, Int. J. Hydrogen Energy 38 (2013) 14189–14199, https://doi.org/10.1016/j.ijhydene.2013.08.119.

[47] A. Mettenbörger, T. Singh, A.P. Singh, T.T. Järvi, M. Moseler, M. Valldor, S. Mathur, Plasma-chemical reduction of iron oxide photoanodes for efficient solar hydrogen production, Int. J. Hydrogen Energy 39 (2014) 4828–4835, https://doi.org/10.1016/j.ijhydene.2014.01.080.

[48] A. Kumar, R. Srivastava, $FeVO_4$ decorated $-SO_3H$ functionalized polyaniline for direct conversion of sucrose to 2,5-diformylfuran & 5-ethoxymethylfurfural and selective oxidation reaction, Mol. Catal. 465 (2019) 68–79, https://doi.org/10.1016/j.mcat.2018.12.017.

[49] Y. Che, G. Feng, W. Guo, J. Xiao, C. Song, Synthesis of $FeVO_4$ nanoparticles and sensing performance for ethanol gas under different solution pH, Cryst. Res. Technol. 56 (2021) 2100110, https://doi.org/10.1002/crat.202100110.

[50] M. Ohno, Effects of Coster-Kronig fluctuation and decay on X-ray photoelectron spectroscopy spectra, J Electron Spectros Relat Phenomena 131–132 (2003) 3–28, https://doi.org/10.1016/S0368-2048(03)00109-9.

[51] B.V. Voloshin, V.A. Seleznev, V.A. Golyashov, Atomic Layer deposition synthesis of thin films of vanadium oxides in a reducing hydrogen atmosphere, J. Struct. Chem. 65 (2024) 2073–2087, https://doi.org/10.1134/S0022476624100160.

[52] G. Kesavan, M. Pichumani, S.M. Chen, Influence of crystalline, structural, and electrochemical properties of iron vanadate nanostructures on flutamide detection, ACS Appl. Nano Mater. 4 (2021) 5883–5894, https://doi.org/10.1021/acsanm.1c00802.

[53] H. Du, J. Wang, Y. Sun, P. Yao, X. Li, N. Yu, Investigation of gas sensing properties of SnO_2/In_2O_3 composite hetero-nanofibers treated by oxygen plasma, Sens Actuators B Chem 206 (2015) 753–763, https://doi.org/10.1016/j.snb.2014.09.010.

[54] T. Wang, T. Liu, W. Li, X. Hao, Q. Lu, H. Yu, X. Liang, F. Liu, F. Liu, C. Wang, G. Lu, Triethylamine sensing with a mixed potential sensor based on $Ce_{0.8}Gd_{0.2}O_{1.95}$ solid

electrolyte and $La_{1-x}Sr_xMnO_3$ (x = 0.1, 0.2, 0.3) sensing electrodes, Sens Actuators B Chem. 327 (2021) 128830, https://doi.org/10.1016/j.snb.2020.128830.
[55] J.W. Peng, P.C. Liu, S. Lee, Reversible band gap tuning of metal oxide films using hydrogen and oxygen plasmas, Thin Solid Films 531 (2013) 81–87, https://doi.org/10.1016/j.tsf.2012.12.044.
[56] A. Bhargava, R. Eppstein, J. Sun, M.A. Smeaton, H. Paik, L.F. Kourkoutis, D. G. Schlom, M. Caspary Toroker, R.D. Robinson, Breakdown of the Small-Polaron Hopping Model in Higher-Order Spinels, Adv. Mater. 32 (2020) 2004490, https://doi.org/10.1002/adma.202004490.
[57] M. Torkamani Cheriani, A. Mirzaei, Plasma-treated nanostructured resistive gas sensors: a review, Sensors 25 (2025) 2307, https://doi.org/10.3390/s25072307.
[58] S.K. Lee, D. Chang, S.W. Kim, Gas sensors based on carbon nanoflake/tin oxide composites for ammonia detection, J. Hazard. Mater. 268 (2014) 110–114, https://doi.org/10.1016/j.jhazmat.2013.12.049.
[59] S. Zolghadr, K. Khojier, S. Kimiagar, Study of sensitivity and selectivity of α-Fe_2O_3 thin films for different toxic gases and alcohols, Mater. Sci. Semicond. Process. 54 (2016) 6–13, https://doi.org/10.1016/j.mssp.2016.06.016.
[60] J.D. Prades, R. Jimenez-Diaz, M. Manzanares, F. Hernandez-Ramirez, A. Cirera, A. Romano-Rodriguez, S. Mathur, J.R. Morante, A model for the response towards oxidizing gases of photoactivated sensors based on individual SnO_2 nanowires, PCCP 11 (2009) 10881–10889, https://doi.org/10.1039/b915646a.
[61] Y. Huang, L. Wieck, S. Tao, Development and evaluation of optical fiber NH_3 sensors for application in air quality monitoring, Atmos. Environ. 66 (2013) 1–7, https://doi.org/10.1016/J.ATMOSENV.2012.06.072.
[62] P. Kanjalkar, J. Kanjalkar, D. Ghuge, K. Ghodake, V. Godase, S. Halbe, An integrated ammonia gas detection and monitoring system for industrial safety and environmental health, in: Advances in Intelligent Systems Research, Atlantis Press, 2025, pp. 64–75, https://doi.org/10.2991/978-94-6463-704-5_7.
[63] B. Yang, X. Li, Z. Hua, Z. Li, X. He, R. Yan, Y. Li, Z. Zhi, C. Tian, A low cost and high performance NH_3 detection system for a harsh agricultural environment, Sens Actuators B Chem 361 (2022) 131675, https://doi.org/10.1016/J.SNB.2022.131675.
[64] M. Navaneethan, V.L. Patil, S. Ponnusamy, C. Muthamizhchelvan, S. Kawasaki, P. S. Patil, Y. Hayakawa, Sensitivity enhancement of ammonia gas sensor based on Ag/ZnO flower and nanoellipsoids at low temperature, Sens Actuators B Chem 255 (2018) 672–683, https://doi.org/10.1016/j.snb.2017.08.015.
[65] R. Sankar ganesh, M. Navaneethan, G.K. Mani, S. Ponnusamy, K. Tsuchiya, C. Muthamizhchelvan, S. Kawasaki, Y. Hayakawa, Influence of Al doping on the structural, morphological, optical, and gas sensing properties of ZnO nanorods, J. Alloys Compd. 698 (2017) 555–564, https://doi.org/10.1016/j.jallcom.2016.12.187.
[66] Z. Li, X. Liu, M. Zhou, S. Zhang, S. Cao, G. Lei, C. Lou, J. Zhang, Plasma-induced oxygen vacancies enabled ultrathin ZnO films for highly sensitive detection of triethylamine, J. Hazard. Mater. 415 (2021) 125757, https://doi.org/10.1016/j.jhazmat.2021.125757.
[67] J. Yang, B.S. Eller, R.J. Nemanich, Surface band bending and band alignment of plasma enhanced atomic layer deposited dielectrics on Ga- and N-face gallium nitride, J. Appl. Phys. 116 (2014) 123702, https://doi.org/10.1063/1.4895985.
[68] C. Shi, J. Liu, W. Li, X. Jiang, H. Yang, Q. Liu, Hydrogen plasma reduction induced oxygen vacancies in cubic In_2O_3 particles with enhanced photocatalytic performance, Ceram. Int. 44 (2018) 22235–22240, https://doi.org/10.1016/j.ceramint.2018.08.343.
[69] L. Wang, S. Chen, W. Li, K. Wang, Z. Lou, G. Shen, Grain-boundary-induced drastic sensing performance enhancement of polycrystalline-microwire printed gas sensors, Adv. Mater. 31 (2019) 1804583, https://doi.org/10.1002/adma.201804583.
[70] N. Barsan, U. Weimar, Conduction model of metal oxide gas sensors, J. Electroceram. 7 (2001) 143–167, https://doi.org/10.1023/A:1014405811371.
[71] X. Xiao, L. Liu, J. Ma, Y. Ren, X. Cheng, Y. Zhu, D. Zhao, A.A. Elzatahry, A. Alghamdi, Y. Deng, Ordered mesoporous tin oxide semiconductors with large pores and crystallized walls for high-performance gas sensing, ACS Appl. Mater. Interfaces 10 (2018) 1871–1880, https://doi.org/10.1021/acsami.7b18830.
[72] A. Reghu, L.J. Legore, J.F. Vetelino, R.J. Lad, B.G. Frederick, Distinguishing bulk conduction from band bending transduction mechanisms in chemiresistive metal oxide gas sensors, J. Phys. Chem. C 122 (2018) 10607–10620, https://doi.org/10.1021/acs.jpcc.8b01446.
[73] M. Hübner, C.E. Simion, A. Tomescu-Stănoiu, S. Pokhrel, N. Bârsan, U. Weimar, Influence of humidity on CO sensing with p-type CuO thick film gas sensors, Sens Actuators B Chem 153 (2011) 347–353, https://doi.org/10.1016/j.snb.2010.10.046.
[74] Y.C. Zhang, Z. Li, L. Zhang, L. Pan, X. Zhang, L. Wang, J.J.Z. Fazal-e-Aleem, Role of oxygen vacancies in photocatalytic water oxidation on ceria oxide: experiment and DFT studies, Appl Catal B 224 (2018) 101–108, https://doi.org/10.1016/j.apcatb.2017.10.049.
[75] A.R. Puigdollers, P. Schlexer, S. Tosoni, G. Pacchioni, Increasing oxide reducibility: the role of metal/oxide interfaces in the formation of oxygen vacancies, ACS Catal. 7 (2017) 6493–6513, https://doi.org/10.1021/acscatal.7b01913.
[76] Y.V. Kaneti, M. Liu, X. Zhang, Y. Bu, Y. Yuan, X. Jiang, A. Yu, Synthesis of platinum-decorated iron vanadate nanorods with excellent sensing performance toward n-butylamine, Sens Actuators B Chem 236 (2016) 173–183, https://doi.org/10.1016/j.snb.2016.05.142.
[77] G. Jeevitha, R. Abhinayaa, D. Mangalaraj, N. Ponpandian, P. Meena, V. Mounasamy, S. Madanagurusamy, Porous reduced graphene oxide (rGO)/WO_3 nanocomposites for the enhanced detection of NH_3 at room temperature, Nanoscale Adv. 1 (2019) 1799, https://doi.org/10.1039/C9NA00048H.
[78] P.G. Su, Y.X. Zheng, A room temperature NH_3 gas sensor based on a quartz crystal microbalance coated with a rGO–SnO_2 composite film, Anal. Methods 14 (2022) 1454–1461, https://doi.org/10.1039/D2AY00283C.
[79] Y. Fu, T. Wang, X. Wang, X. Li, Y. Zhao, F. Li, G. Zhao, X. Xu, Investigation of p-n sensing transition and related highly sensitive NH_3 gas sensing behavior of SnP_x/rGO composites, Chem. Eng. J. 471 (2023) 144499, https://doi.org/10.1016/J.CEJ.2023.144499.
[80] S. Singh, K.Y. Shin, S. Moon, S.S. Kim, H.W. Kim, Phase-engineered $MoSe_2$/CeO_2 composites for room-temperature gas sensing with a drastic discrimination of NH_3 and TEA gases, ACS Sens 9 (2024) 3994–4006, https://doi.org/10.1021/acssensors.4c00793.
[81] T.T.H. Duong, H.H. Hau, L.T. Hong, L.A. Vu, C.M. Hung, N. Van Duy, N. Van Hieu, N.D. Hoa, PtO_2-decorated MoS_2 ultrathin nanostructures for enhanced NH_3 gas sensing properties, Mater. Sci. Semicond. Process. 151 (2022) 106990, https://doi.org/10.1016/j.mssp.2022.106990.
[82] T. Jrvinen, G.S. Lorite, J. Per ntie, G. Toth, S. Saarakkala, V.K. Virtanen, K. Kordas, WS_2 and MoS_2 thin film gas sensors with high response to NH_3 in air at low temperature, Nanotechnology 30 (2019) 405501, https://doi.org/10.1088/1361-6528/ab2d48.
[83] S. Kumar, A. Singh, R. Singh, S. Singh, P. Kumar, R. Kumar, Facile h-MoO_3 synthesis for NH_3 gas sensing application at moderate operating temperature, Sens Actuators B Chem 325 (2020) 128974, https://doi.org/10.1016/J.SNB.2020.128974.
[84] P. Gouma, K. Kalyanasundaram, X. Yun, M. Stanaćević, L. Wang, Nanosensor and breath analyzer for ammonia detection in exhaled human breath, IEEE Sens. J. 10 (2010) 49–53, https://doi.org/10.1109/JSEN.2009.2036050.
[85] K.S. Mohammed, J. ALzanganawee, A.A. Kamil, Optimizing ZnO–SnO_2 thin-film ratios for high sensitivity to NO_2 and NH_3, J. Mater. Sci. Mater. Electron. 36 (2025) 1381, https://doi.org/10.1007/S10854-025-15286-W.
[86] M.M. Tsai, C.T. Lee, M.J. Wu, T.C. Chang, Y.F. Tung, H.Y. Lee, Heterostructured NO_2 gas sensors using decorated p-type reduced graphene oxide nanoparticles on surface modified n-type ZnO nanorods, IEEE Sens. J. 25 (2025) 9393–9400, https://doi.org/10.1109/JSEN.2025.3538865.